COVER SHEET

Paper Number: **28327**

Title: **Effect of unit cell geometry and fiber waviness on the overall mechanical response of 3D woven composites**

Authors: Adam Ewert
Higor Galdino da Silva
Kostiantyn Vasylevskyi
Igor Tsukrov
Borys Drach

ABSTRACT

Effects of two meso-scale geometry generation approaches on finite element predictions effective elastic properties of an orthogonal 3D woven composite are studied in this paper. In particular, one model is created by simulating the weaving process in the software DFMA (Kansas State University). The second model is created by directly processing X-ray microtomography (μCT) data. Experimental measurements of transverse Young's moduli are used to inform the accuracy of the predicted elastic results.

In both cases, a unit cell with in-plane periodic boundary conditions is modeled, which has not been previously done in the case of μCT-based models. The effect of high frequency oscillations in tow element orientations imparted by a wavy centerline (artifact of μCT image processing) on the elastic properties is studied. The μCT-based model is then used to simulate tension-to-failure.

Adam Ewert, Higor Galdino da Silva, Borys Drach, New Mexico State University, Department of Mechanical and Aerospace Engineering, 1040 S. Horseshoe Str., Las Cruces, NM 88003, U.S.A.

Kostiantyn Vasylevskyi, Igor Tsukrov, University of New Hampshire, Department of Mechanical Engineering, 33 Academic Way, Durham, NH 03824, U.S.A..

INTRODUCTION

Advantages offered by 3D woven composite materials (e.g. high delamination resistance, good impact resistance, and dimensional stability) have led to their increasing use in the aerospace and other performance driven industries [1]. As the demand for 3D woven composites increases, understanding how their design affects elastic and strength properties becomes more important for creating better and safer composites.

Exploring new composite designs experimentally is both time consuming and expensive. Moreover, measuring some properties like out of plane stiffness modulus and shear modulus can be hard if not impossible, creating the need for predictive modeling. This motivates interest in quantifying how meso-scale defects influence predictions of effective elastic and strength properties from high fidelity finite element analysis (FEA).

Several different methods exist to create the desired geometry of a composite unit cell (UC) for virtual testing. The easiest way to create geometry is by describing the desired weave pattern using fiber bundles (tows) with a constant cross section (see, for example, [4, 5, 6]). This ideal, or nominal, method does not capture the variation inherent in the manufacturing process and often does not match the experimentally measured volume fraction of fibers [5]. The digital element method (DE) has been developed to capture the subtleties of tow variation. DE-based models allow for better characterization of resulting tow shape from the weaving process by simulating multiple threads per tow and their interactions [5, 6, 7]. As tension is applied to tows, the tows interact and their cross sections are subjected to non-uniform transverse deformation. This method often leads to overlapping of tow geometries, which must be corrected before analysis can be performed.

Alternatively, 3D woven geometry can be obtained from X-ray microtomography (μCT) or serial sectioning using optical microscopy of an existing specimen to capture a volumetric point cloud representing the reinforcement. The point cloud is constructed from multiple images, each representing a slice of the material. μCT-based models are the most accurate virtual representations of the composite material as they are reconstructed data from an actual specimen [9]. This makes them especially valuable for calibration of other geometry generation techniques.

While there are many studies concerning the prediction of elastic properties of 3D woven fabrics, most of them simplify meso-scale geometry for ease of homogenization. Comparative studies, like Liu et al. [10], do not always use consistent boundary conditions to compare simulated and imaging-based models. To our knowledge, direct comparison between simulated tow mesh based on weave process simulations, μCT-based, and experimental data has not been performed. Each model studied in this paper employs periodic boundary conditions over a single representative UC, which has not been previously done in the case of μCT-based meshes. The goal of this study is to determine the effect meso-scale geometry generation approaches have on predicting effective elastic properties using FEA. Experimental results obtained by Vyshenska [11] ranging from 72.3 GPa to 84.12 GPa in the warp direction and 60.8 GPa to 70.78 GPa in the weft direction are used to inform the accuracy of the predictions made from FEA. The average values for each range, 77.3 GPa in warp and 65.8 GPa in weft, are used for comparison.

The paper is organized as follows. First, the methodology of geometry generation using a digitally simulated weaving approach, and mesh generation based on X-ray microtomography is discussed. Then the differences in the geometries are compared. Next, the material properties used and details of the periodic boundary conditions as well as the methodology for determining the effective elastic properties are presented. The impact of small oscillations on effective elastic properties in the μCT-based are shown and compared to the simulated mesh. Finally, uniaxial tension-to-failure is simulated using the μCT-based model.

GEOMETRY AND MESH PREPARATION METHODOLOGY

Digital Fabric Mechanics Approach

One of the one-to-one orthogonal meshes used in this paper is generated using Digital Fabric Mechanics Analyzer (DFMA), digital element method software developed at Kansas State University [6]. Characteristics of the considered UC such as number of warp and weft layers, weave pattern, and cross-sectional area of the tows are used as inputs to begin the modeling process. The initial pattern of individual tows represented as cylinders as shown in Figure 1a is generated by the software. The tows are then subdivided into bundles of digital elements subjected to tensile forces, which results in contact interaction of these elements creating non-uniform cross sections, see Figure 1b. Using this process the "DFMA" model was created for our analysis. Expected area of tow cross section based on the number of fibers, fiber diameter, and fiber volume fraction in each tow were used.

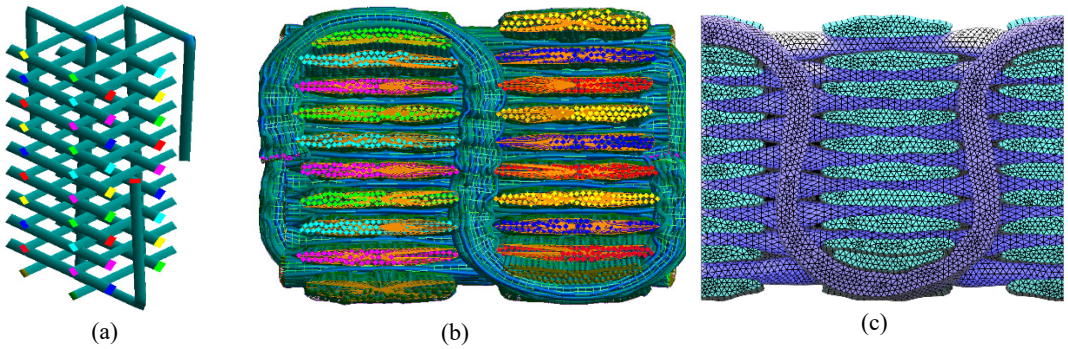

Figure 1. Abbreviated DFMA workflow: (a) initial weave pattern represented by cylindrical tows; (b) tows represented by bundles of digital element chains; (c) FEA-ready volumetric mesh of the composite unit cell (matrix mesh is hidden)

The final deformed fabric is exported from DFMA as a point cloud and further processed to create an FEA ready mesh using a previously developed procedure [12]. We noticed that in the model generated using the DFMA process described above, the weft tows' volume fraction is higher than the warp tows' volume fraction, which is opposite from the manufactured specimen, compare volume fractions of "DFMA" with "μCT" in Table 1. Volume fractions in the latter column correspond to values of the microtomography-based model.

Table 1. Volume fractions of different tow types in DFMA and μCT meshes, %

	DFMA	**μCT**
$V_{f\,warp}$	26.6	31.6
$V_{f\,weft}$	33.3	29.0
$V_{f\,binder}$	8.42	6.76
$V_{f\,total}$	68.3	67.4

The final geometry is meshed with volumetric tetrahedral four-node (tet-4) elements. With the DFMA point cloud, center points along each tow are included. These center points are used to create material orientation vectors for each element with the primary direction aligned along the tow direction. Once material orientations are assigned, the volume elements are converted to tetrahedral ten-node (tet-10) elements. The final "DFMA" model contains 788,182 nodes and 558,587 elements.

Microtomography Approach

Using μCT of a one-to-one orthogonal architecture of carbon fiber/epoxy matrix composite, a 3D conformal mesh was generated. While the data encompasses more than one complete unit cell, only a quarter of a unit cell could be confidently used, see Figure 2. This is due to a misplaced binder tow in the μCT data set causing irregularities in a large portion of the data. The quarter unit cell is mirrored to create a full unit cell after further processing.

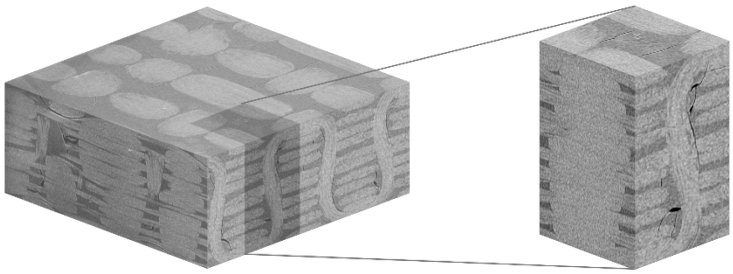

(a) (b)

Figure 2. Microtomography data: (a) full dataset and (b) section selected for tow geometry extraction

Segmentation of the selected portion of the μCT data required to separate the tows from the matrix was performed in ImageJ. Contrast between the matrix and the tow materials is low and the data is very noisy, which prohibited an automated segmentation process. As such, tow profiles were traced manually; the final surface mesh shown in Figure 3 was exported from ImageJ for further processing. While tracing tows, a slight gap was intentionally left between the tows that appeared to be touching. This was done because overlapping elements in the conformal mesh are not allowed in our procedure. For a better control over mesh density and trimming of the

tows to unit cell dimensions, a non-uniform rational basis spline (NURBS) surface was generated for each tow using vertices from the STL files.

(a) (b)

Figure 3. Warp tows: (a) filled with a solid color as shown in the selected portion of the μCT data; (b) extracted surfaces

After creating and trimming the NURBS surfaces, centerline points are created based on averaged tow profiles for later material orientation assignment. After orientations are assigned, tet-4 elements are converted to tet-10 elements. The final tetrahedral mesh used for analysis contains 843,378 nodes and 616,101 elements. This procedure resulted in the "Original μCT" model.

Comparison of Tow Geometries between DFMA- and μCT-Based Meshes

Compared to the nominal geometry, the DE method can more accurately simulate defects imparted by the weaving process, there are still some effects, like compaction, that are not captured accurately, see Figure 4. The μCT-based model can be seen to be flatter on the top and bottom, whereas the top and bottom surfaces of the DFMA mesh are still rounded. Slight differences in the warp and weft tows can also be seen as there is more variation in shape in the μCT-based model.

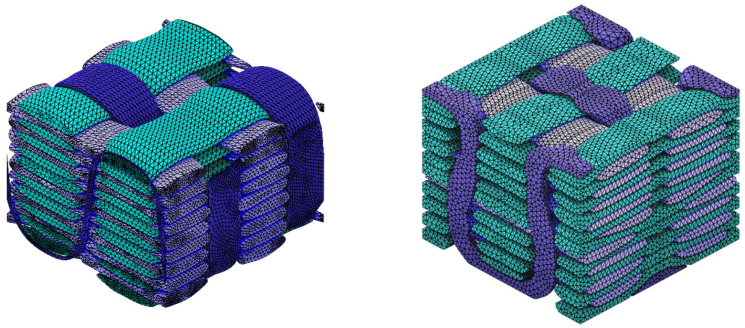

(a) (b)

Figure 4. Final reinforcement meshes: (a) "DMFA"; (b) extracted from μCT data

In the "DFMA" model, excessive pinching can be seen in the warp tows, see Figure 5. As the warp tows are held under tension in the weaving process, this is not seen in the μCT mesh and may have an impact on predicted effective elastic properties as discussed further. In addition to a flatter top and bottom, the binder tow

takes on a more pronounced 'S' shape as the fabric is compacted. This effect is not captured at all in the "DFMA" model. It is expected that a straighter binder tow would artificially stiffen the through-thickness effective elastic properties.

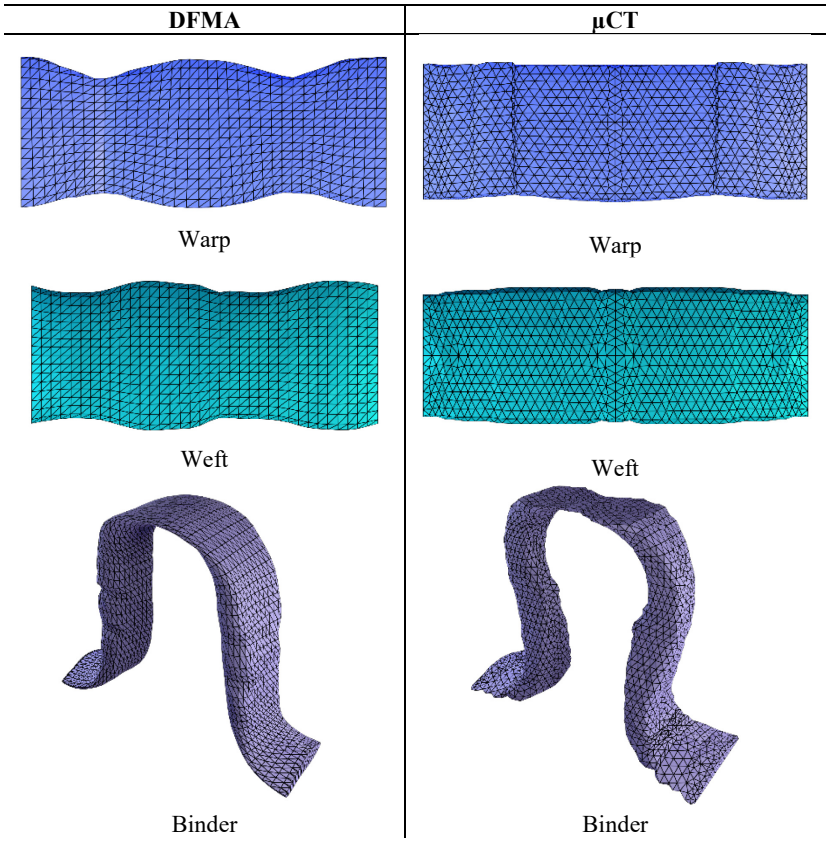

Figure 5. Comparison of tows shapes between the considered models

FINITE ELEMENT ANALYSIS: MODEL PREPARATION AND PROCESSING

Material Properties

The FEA package MSC Marc (https://www.mscsoftware.com/product/marc) is used for simulations in this paper. The matrix is modeled as linearly elastic having the properties of the HEXCEL RTM6 epoxy resin with Young's modulus, $E_m = 2.89\ GPa$, Poisson's ratio of $\nu_m = 0.35$ [13]. The tows are bundles of 12,000 IM7 carbon fibers impregnated with RTM6 epoxy with fiber volume fraction of $V_f = 80\%$ [12]. They are modeled as homogenized transversely isotropic solids with effective elastic properties calculated from the equations presented in [7, 6, 23] using manufacturer specified fiber properties [14]. The elastic properties are summarized in Table 2.

Table 2. Carbon fiber and effective tow properties

Material	E_1 (GPa)	E_2 (GPa)	G_{12} (GPa)	ν_{12}	ν_{23}
IM7 carbon fiber	276	23.1	27.6	0.350	0.300
RTM6 epoxy + IM7 carbon fibers ($Vf = 80\%$)	221	13.18	7.17	0.350	0.350

Periodic Boundary Conditions

Periodic boundary conditions are applied in the warp and weft directions, the x- and y-directions respectively. The through-thickness, z-direction, of the unit cell is assumed to represent the total thickness of the specimen and does not require periodic boundary conditions to be applied. Boundary conditions in the meso-scale unit cell preserve material continuity on the macroscale. The displacements are described using the following formulation:

$$\underline{\mathbf{u}}_i^+ = \underline{\mathbf{u}}_i^- + \underline{\boldsymbol{\delta}}_i \quad (i = warp, weft) \tag{1}$$

where $\underline{\mathbf{u}}_i^+$ and $\underline{\mathbf{u}}_i^-$ are the vectors of nodal displacements on the positive and negative faces, and $\underline{\boldsymbol{\delta}}_i$ is the vector of prescribed displacements in the *i*-th direction.

Processing of Simulation Results

The orthogonal DFMA- and μCT-based models are subjected to uniaxial and shear mechanical loading to determine the effective properties by relating applied macroscopic strains with volume-averaged stresses, see [12]. Volume-averaged stress values are extracted from the results of the numerical simulations using a custom Python script as follows:

$$\langle \sigma_{ij} \rangle_m = \frac{1}{V} \sum_{l=1}^{N_e} \left(\sigma_{ij}^{(l)} \right)_m \cdot V^{(l)}, \quad i,j = 1,2,3 \tag{2}$$

where $\langle \sigma_{ij} \rangle_m$ is the volume average of the stress component ij calculated from the m-th load case, V is the UC volume, $\left(\sigma_{ij}^{(l)} \right)_m$ is the stress component ij at the centroid of the finite element l calculated from the m-th load case, $V^{(l)}$ is the volume of the element l, and N_e is the total number of elements in the model. The overall material stiffness components C_{ijkl}^{eff} are found as the proportionality coefficients relating macroscopic strains with volume-averaged stresses. For example, in the first load case (tension in x direction): $C_{ijkl}^{eff} \cdot (\varepsilon_{kl}^0)_1 = \langle \sigma_{ij} \rangle_1$ $(i,j,k,l = 1,2,3)$; there is only one non-zero component of applied strain $(\varepsilon_{11}^0)_1$ which can be used to obtain stiffness components C_{ij11}^{eff} [15]:

$$C_{ij11}^{eff} = \frac{\langle \sigma_{ij} \rangle_1}{\left(\varepsilon_{11}^0\right)_1} \quad (3)$$

RESULTS AND DISCUSSIONS

Effect of Small Oscillations in Material Orientations

The overall elastic properties of the μCT-based model, along with the experimental results [11] are presented in Table 3. Initial FEA results from "Original μCT" geometry are 20% and 32% less stiff in the warp and weft directions respectively compared to the averaged experimental results. Investigation into the source of the discrepancy in the stiffness revealed that the generated centerlines used to assign local material orientations exhibit high frequency waviness, see Figure 6.

Table 3. Overall elastic properties of the μCT-based models

	Original μCT	**Avg μCT**	**Experimental results** [11]
$E_{1\,(warp)}$, GPa	61.7	72.4	77.3
$E_{2\,(weft)}$, GPa	44.8	61.1	65.8
$E_{3\,(binder)}$, GPa	11.3	11.7	
G_{12}, GPa	4.55	4.31	
G_{23}, GPa	2.87	2.87	
G_{13}, GPa	2.94	2.90	

Due to the manufacturing process involving pre-tensioning the fibers, this waviness is not expected and is not observed in μCT data of manufactured physical specimens. To more closely approximate the expected shape of the fiber, the centerline points were smoothed via running average (with six points) thus decreasing the average directional change between centerline points, see Figure 6. Thus, the "Original μCT" and "Avg μCT" models are identical in all properties except local material orientations. With smoother centerlines, the FEA results more closely approximate the average moduli obtained experimentally – the "Avg μCT" results are only 6% and 7% less stiff in the warp and weft directions respectively. Potential sources of the difference include presence of the artificial gaps between the tows in the FEA model and geometric variations between unit cells within the composite. Processing of additional μCT data obtained for the same composite architecture should help improve our models' accuracy. The following sections will reference the "Avg μCT" results when making comparisons.

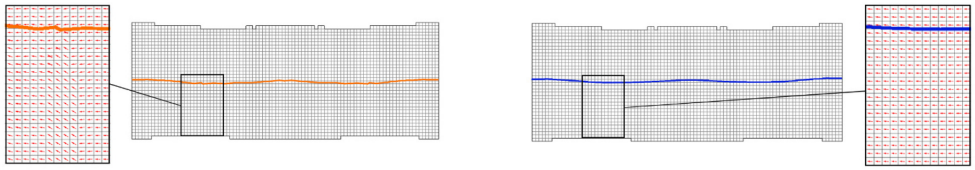

(a) (b)

Figure 6. Comparison of local material orientations (uniform hex elements are presented for visual clarity): (a) before averaging; (b) after averaging

Comparison of Overall Elastic Responses of DFMA- and µCT-Based Unit Cells

Results for the "DFMA" model show a lower Young's modulus in the warp direction at 57.4 GPa compared to 67.7 GPa in the weft direction. Experimentally, average Young's modulus in the warp direction is higher than the modulus in the weft direction, 77.3 GPa vs 65.8 GPa, respectively. While the warp and weft stiffness of the "DFMA" model varies greatly from the "Avg µCT" model, the binder direction Young's modulus matches exactly, see Table 4.

Table 4. Overall elastic properties of the DFMA- and µCT-based models

	DFMA	**Avg µCT**	**Experimental results** [11]
$E_{1\,(warp)}$, GPa	57.4	72.4	77.3
$E_{2\,(weft)}$, GPa	67.7	61.1	65.8
$E_{3\,(binder)}$, GPa	11.7	11.7	
G_{12}, GPa	4.36	4.31	
G_{23}, GPa	2.97	2.87	
G_{13}, GPa	3.1	2.90	

Simulation of Tension-to-Failure

Predicting the strength of composite materials is difficult due to complex interactions between fiber reinforcement and the matrix. In this section, a preliminary simulation of tension-to-failure in the warp direction of the µCT model is presented. Tension-to-failure of a 3D woven composite with a similar orthogonal reinforcement architecture has recently been simulated and reported in [16].

The well-known failure-mode-based Hashin criterion ([17], [18]) is used for characterizing the strength of tows, see Table 5 for properties used in this study. Progressive failure is modeled by gradually reducing the tow stiffness to keep the failure indices equal to 1.0 after failure is initiated.

Table 5. Strength properties of IM7/RTM6 ([14], [19])

X_t (MPa)	X_c (MPa)	Y_t (MPa)	Y_c (MPa)	S_{12} (MPa)	S_{23} (MPa)
5313	-1862	90	-320	100	100

The failure criterion used for the bulk matrix combines equivalent plastic strain, von Mises stress and hydrostatic stress:

$$p_e - ae^{-b\frac{\sigma_{vm}}{\sigma_H}} - c = 0 \tag{4}$$

where p_e is the equivalent plastic strain, σ_{vm} is the von Mises stress, σ_H is the hydrostatic stress, and a, b, and c are parameters identified based on experimental data (see [20]): $a = 0.04042$, $b = 7.815$, and $c = 0.02558$. The criterion and plastic behavior of the matrix are based on room temperature results from [20].

To characterize the progressive failure of the bulk matrix the smeared crack approach is chosen. The smeared crack approach, originally developed for concrete, is a damage model that characterizes microcracking in a brittle material [21]. Its advantages allow for cracking to be mesh independent because the dissipation energy can be adjusted based on the element size. Since fully cured RTM6 resin is brittle and susceptible to microcracking, the smeared crack approach is an appropriate choice for characterization. Morelle et al. [20] shows good correlation between the simulated and the experimental Iosipescu tests on pure epoxy.

The stress-strain curve of the tension-to-failure numerical experiment is presented in Figure 7. Non-linear behavior is observed at a stress of 347 MPa and strain of 0.0049. The maximum stress of 453 MPa corresponding to a strain of 0.0071 is observed. The ultimate stress of 435 MPa and strain of 0.007576 so far cannot be determined to be the true ultimate stress and strain because of poor simulation convergence.

Stress is mainly carried through the warp tows and not the matrix, see Figure 8. The portion of the binder tows parallel to the warp tows also carry some of the load. The fiber tension failure mode is mostly seen on the warp tows as they are carrying the majority of the load, Figure 9a. However, the matrix tension failure mode is seen in warp, weft, and binder tows, Figure 9b.

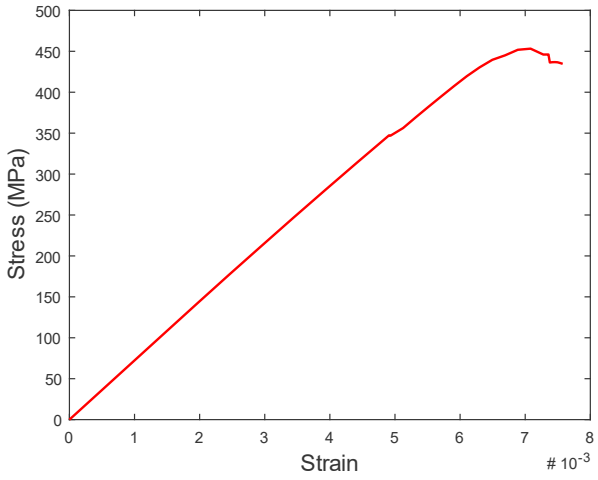

Figure 7. Stress vs Strain in the x-direction

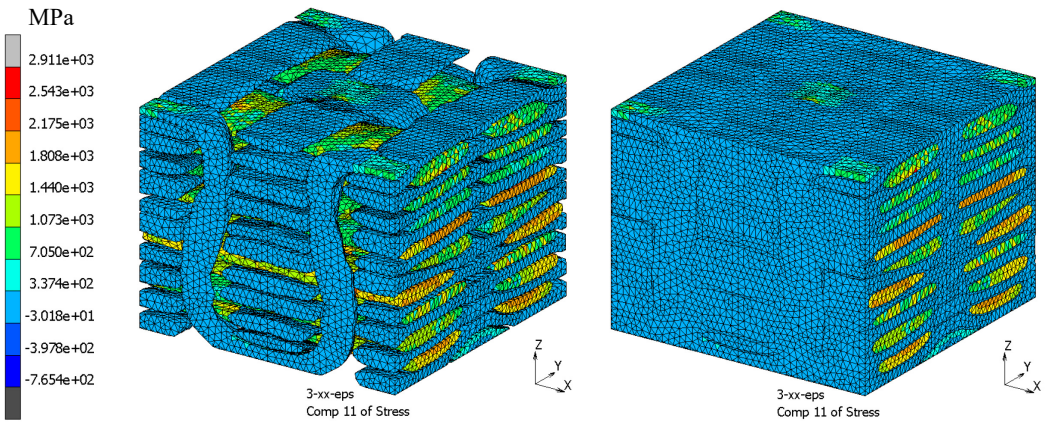

(a) (b)

Figure 8. Ultimate stress in x-direction: (a) tows only, (b) with matrix

Failure of the tow elements in both fiber and matrix tension modes corresponds to key points in the stress curve, Figure 10. A sharp increase in the normalized V_{fF_3} (volume fraction of the failure index 3 corresponding to tensile matrix failure) seen at an applied strain of 0.00491 corresponds to the beginning of the non-linear behavior, see Figure 10a. This shows the accumulation of damage and the effect progressive softening in the elements has on the overall strength response. Just after maximum stress, elements begin to fail in the fiber tension mode, where normalized V_{fF_1} (volume fraction of the failure index 1 corresponding to tensile fiber failure) starts to increase sharply. As the elements soften in the longitudinal direction, the model quickly fails. The bulk matrix experiences almost no failure in this analysis.

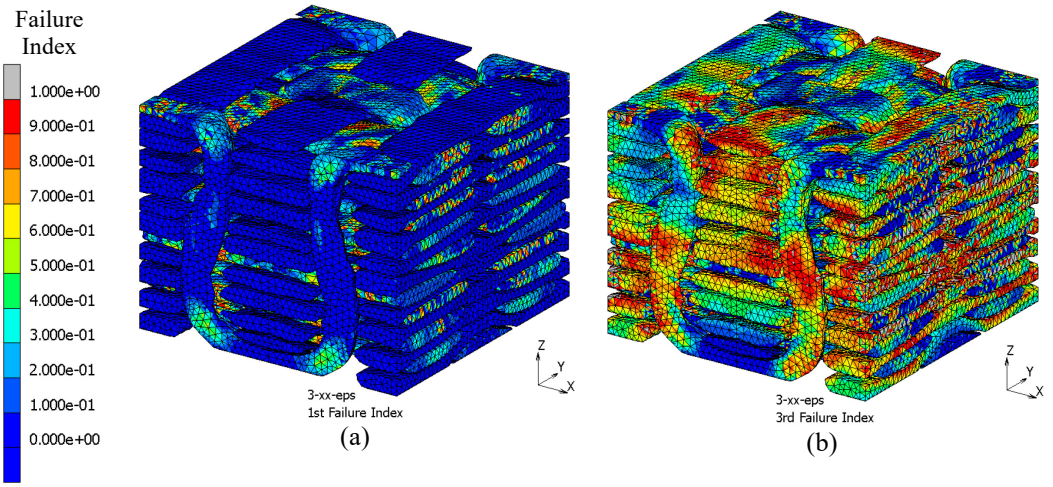

(a) (b)

Figure 9. Hashin failure criterion in tows (hidden matrix) at ultimate stress: (a) first failure index (fibers in tension), (b) third failure index (matrix in tension)

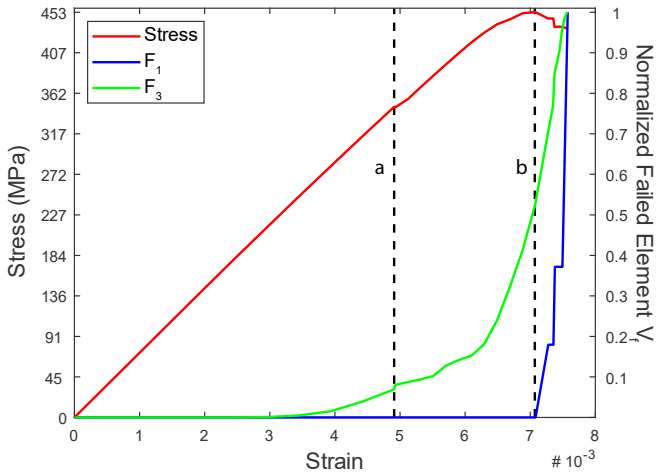

Figure 10. Normalized volume fraction of failed elements where (a) non-linear behavior corresponds to increase in failure index F_3 and (b) where an increase in failure index F_1 corresponds to maximum failure

CONCLUSIONS

Two mesh generation techniques for meso-scale FEA of a carbon/epoxy one-to-one orthogonal 3D woven composite are evaluated by comparing FEA predictions of the overall Young's moduli to experimental results. The techniques studied are simulated fabric weaving using DFMA and a model based on image processing of μCT data of a physical specimen. Tow shape, local material orientations, and volume fractions vary between models and have different effects on the predicted properties. The method for creating the μCT-based model is demonstrated to be robust enough to allow for the implementation of periodic boundary conditions.

DFMA model predictions show greater Young's modulus in the weft direction than in the warp direction. This trend is opposite to the experimentally observed. DFMA model also appears to significantly underpredict the warp Young's modulus.

It is shown that high frequency oscillations in tow element orientations imparted by a wavy centerline (an artifact of microtomography image processing) significantly reduce the predicted Young's moduli in the warp and weft directions. In contrast, the oscillating material orientations do not affect the predicted shear moduli. With averaged centerlines, the "Avg μCT" model's warp and weft elastic property predictions show good correspondence with the experimental results.

Simulation of tension-to-failure of the "Avg μCT" model shows that matrix tension failure of the tows leads to a non-linear behavior in the stress curve. Even though most of the matrix failed in the tows, the bulk matrix experienced almost no failure. This may be explained in part by two different failure criteria used for bulk and intra-tow matrix – in the former the criterion is based on combination of equivalent plastic strain, von Mises and hydrostatic stress, and in the latter the criterion is only based on equivalent stress. In addition, the material model for the intra-tow matrix does not incorporate plasticity. In the tows, elements begin to completely fail in the fiber tension mode where the maximum stress is reached. Once elements fail in this mode, the model exhibits a rapidly accelerating softening. Further investigation into the failure criteria and other damage approaches is needed to determine the quality of the results.

ACKNOWLEDGEMENTS

This material is based upon work supported by the National Science Foundation under Grant No. CMMI-1662098. The financial support of the New Mexico Space Grant Consortium through the NASA Cooperative Agreement NNX15AK41A is gratefully acknowledged.

REFERENCES

[1] T. Huang, Y. Wang, and G. Wang, "Review of the Mechanical Properties of a 3D Woven Composite and Its Applications," *Polym. - Plast. Technol. Eng.*, vol. 57, no. 8, pp. 740–756, 2018.

[2] H. Lin, L. P. Brown, and A. C. Long, "Modelling and Simulating Textile Structures Using TexGen," *Adv. Mater. Res.*, vol. 331, pp. 44–47, Sep. 2011.

[3] I. Tsukrov *et al.*, "Finite Element Modeling to Predict Cure-Induced Microcracking in Three-Dimensional Woven Composites," *Int. J. Fract.*, vol. 172, no. 2, pp. 209–216, Dec. 2011.

[4] D. Kuksenko, H. J. Böhm, and B. Drach, "Effect of micromechanical parameters of composites with wavy fibers on their effective response under large deformations," *Adv. Eng. Softw.*, vol. 121, pp. 206–222, Jul. 2018.

[5] A. Doitrand, C. Fagiano, F. X. Irisarri, and M. Hirsekorn, "Comparison between voxel and consistent meso-scale models of woven composites," *Compos. Part A Appl. Sci. Manuf.*, vol. 73, pp. 143–154, 2015.

[6] G. Zhou, X. Sun, and Y. Wang, "Multi-chain digital element analysis in textile mechanics," *Compos. Sci. Technol.*, vol. 64, no. 2, pp. 239–244, Feb. 2004.

[7] L. Huang, Y. Wang, Y. Miao, D. Swenson, Y. Ma, and C. F. Yen, "Dynamic relaxation approach with periodic boundary conditions in determining the 3-D woven textile micro-geometry," *Compos. Struct.*, vol. 106, pp. 417–425, 2013.

[8] L. Daelemans *et al.*, "Finite element simulation of the woven geometry and mechanical behaviour of a 3D woven dry fabric under tensile and shear loading using the digital element method," *Compos. Sci. Technol.*, vol. 137, pp. 177–187, 2016.

[9] S. C. Garcea, Y. Wang, and P. J. Withers, "X-ray computed tomography of polymer composites," *Compos. Sci. Technol.*, vol. 156, pp. 305–319, 2018.

[10] Y. Liu, I. Straumit, D. Vasiukov, S. V. Lomov, and S. Panier, "Prediction of linear and non-linear behavior of 3D woven composite using mesoscopic voxel models reconstructed from X-ray micro-tomography," *Compos. Struct.*, vol. 179, pp. 568–579, 2017.

[11] K. Vyshenska, "Thesis: Numerical and Experimental Studies of Mechanical Behavior and Cure Induced Stresses in 3D Carbon/Epoxy Composites," University of New Hampshire, 2014.

[12] A. Drach, B. Drach, and I. Tsukrov, "Processing of fiber architecture data for finite element modeling of 3D woven composites Dedicated to Professor Zdeněk Bittnar in occasion of his 70th birthday.," *Adv. Eng. Softw.*, vol. 72, pp. 18–27, 2014.

[13] "https://www.hexcel.com/user_area/content_media/raw/HexFlowRTM6DataSheetPDF.pdf," *Hexcel Corp. Accessed 20 Novemb. 2018*.

[14] "https://www.hexcel.com/user_area/content_media/raw/IM7_HexTow_DataSheet.pdf," *Hexcel Corporation, Accessed: 20 November 2018*. https://www.hexcel.com/user_area/content_media/raw/IM7_HexTow_DataSheet.pdf.

[15] B. Drach, I. Tsukrov, and A. Trofimov, "Comparison of full field and single pore approaches to homogenization of linearly elastic materials with pores of regular and irregular shapes," *Int. J. Solids Struct.*, vol. 96, pp. 48–63, Oct. 2016.

[16] D. K. Patel and A. M. Waas, "Damage and failure modelling of hybrid three-dimensional textile composites: a mesh objective multi-scale approach," *Philos. Trans. R. Soc. A Math. Phys. Eng. Sci.*, vol. 374, no. 2071, p. 20160036, 2016.

[17] I. Daniel and O. Ishai, *Engineering Mechanics of Composite Materials*, Second. Oxford University Press, 2005.

[18] M. Koc, F. O. Sonmez, N. Ersoy, and K. Cinar, "Failure behavior of composite laminates under four-point bending," 2016.

[19] W. D. B. Nairn, John A, Sheila I. Harper, "Effects of Fiber, Matrix, and Interphase on Carbon Fiber Composite Compression Strength," *NASA Contract. Rep. 4601*, 1994.

[20] X. P. Morelle, J. Chevalier, C. Bailly, T. Pardoen, and F. Lani, "Mechanical characterization and modeling of the deformation and failure of the highly crosslinked RTM6 epoxy resin," *Mech Time-Depend Mater*, vol. 21, no. 3, pp. 419–454, 2017.

[21] J. G. Rots, P. Nauta, G. M. A. Kusters, and J. Blaauwendraad, "Smeared Crack Approach and Fracture Localization in Concrete.," *Heron*, vol. 30, no. 1, 1985.